

Excitation strategies for optical lattice microscopy

Eric Betzig

New Millennium Research, LLC
2174 Butternut Dr, Okemos, MI 48864
EricB@chartermi.net

Abstract: Recently, new classes of optical lattices were identified, permitting the creation of arbitrarily large two- and three-dimensional arrays of tightly confined excitation maxima of controllable periodicity and polarization from the superposition of a finite set of plane waves. Here, experimental methods for the generation of such lattices are considered theoretically in light of their potential applications, including high resolution dynamic live cell imaging, photonic crystal fabrication, and quantum simulation and quantum computation using ultracold atoms.

©2005 Optical Society of America

OCIS codes: (020.7010) Trapping; (050.1960) Diffraction theory; (180.6900) 3D microscopy

References and links

1. J. Zhang, R.E. Campbell, A.Y. Ting, and R.Y. Tsien, "Creating new fluorescent probes for cell biology," *Nat. Rev. Mol. Cell Biol.* **3**, 906-918 (2002).
2. D. Axelrod, "Total internal fluorescence microscopy," in *Methods in Cellular Imaging*, A. Periasamy, ed., American Physiological Society Book Series (Oxford Univ. Press, 2001).
3. G.E. Cragg and P.T.C. So, "Lateral resolution enhancement with standing evanescent waves," *Opt. Lett.* **25**, 46-48 (2000).
4. S.W. Hell and J. Wichmann, "Breaking the diffraction resolution limit by stimulated emission: stimulated-emission-depletion fluorescence microscopy," *Opt. Lett.* **19**, 780-782 (1994).
5. C.Y. Dong, P.T.C. So, C. Buehler, and E. Gratton, "Spatial resolution in scanning pump-probe fluorescence microscopy," *Optik* **106**, 7-14 (1997).
6. LZ. Cai, X.L. Wang, and Y.R. Wang, "All fourteen Bravais lattices can be formed by interference of four noncoplanar beams," *Opt. Lett.* **27**, 900-902 (2002).
7. L. Yuan, G.P. Wang, and X. Huang, "Arrangements of four beams for any Bravais lattice," *Opt. Lett.* **28**, 1769-1771 (2003).
8. B. Bailey, D.L. Farkas, D.L. Taylor, and F. Lanni, "Enhancement of axial resolution in fluorescence microscopy by standing-wave excitation," *Nature* **366**, 44-48 (1993).
9. M.A.A. Neil, R. Juskaitis, and T. Wilson, "Method of obtaining optical sectioning by using structured light in a conventional microscope," *Opt. Lett.* **22**, 1905-1907 (1997).
10. M.G.L. Gustafsson, D.A. Agard, and J.W. Sedat, "I5M: 3D widefield light microscopy with better than 100 nm axial resolution," *J. Microsc.* **195**, 10-16 (1999).
11. M.G.L. Gustafsson, "Surpassing the lateral resolution limit by a factor of two using structured illumination microscopy," *J. Microsc.* **198**, 82-87 (2000).
12. J.T. Frohn, H.F. Knapp, and A. Stemmer, "True optical resolution beyond the Rayleigh limit achieved by standing wave illumination," *Proc. Natl. Acad. Sci. USA* **97**, 7232-7236 (2000).
13. V. Berger, O. Gauthier-Lafaye, and E. Costard, "Photonic band gaps and holography," *J. Appl. Phys.* **82**, 60-64 (1997).
14. M. Campbell, D.N. Sharp, M.T. Harrison, R.G. Denning, and A.J. Turberfield, "Fabrication of photonic crystals for the visible spectrum by holographic lithography," *Nature* **404**, 53-56 (2000).
15. D.C. Meisel, M. Wegener, and K. Busch, "Three-dimensional photonic crystals by holographic lithography using the umbrella configuration: Symmetries and complete photonic band gaps," *Phys. Rev. B* **70**, 165104 (2004).
16. P.S. Jessen, *et al.*, "Observation of quantized motion of Rb atoms in an optical field," *Phys. Rev. Lett.* **69**, 49-52 (1992).
17. A. Hemmerich and T.W. Hänsch, "Two-dimensional atomic crystal bound by light," *Phys. Rev. Lett.* **70**, 410-413 (1993).

18. G. Grynberg, B. Lounis, P. Verkerk, J.-Y. Courtois, and C. Salomon, "Quantized motion of cold cesium atoms in two- and three-dimensional optical potentials," *Phys. Rev. Lett.* **70**, 2249-2252 (1993).
19. M. Greiner, O. Mandel, T. Esslinger, T.W. Hänsch, I. Bloch, "Quantum phase transition from a superfluid to a Mott insulator in a gas of ultracold atoms," *Nature* **415**, 39 (2002).
20. J.I. Cirac and P. Zoller, "How to manipulate cold atoms," *Science* **301**, 176-177 (2003).
21. R. Dumke, *et al.*, "Micro-optical realization of arrays of selectively addressable dipole traps: A scalable configuration for quantum computation with atomic qubits," *Phys. Rev. Lett.* **89**, 097903 (2002).
22. J.I. Cirac and P. Zoller, "New frontiers in quantum information with atoms and ions," *Phys. Today* **57**, No. 3, 38-44 (2004).
23. K.I. Petsas, A.B. Coates, and G. Grynberg, "Crystallography of optical lattices," *Phys. Rev. A* **50**, 5173-5189 (1994).
24. E. Betzig, New Millennium Research, LLC, Okemos, MI 48864 has submitted a paper entitled "Sparse and composite coherent lattices".
25. E. Betzig, New Millennium Research, LLC, Okemos, MI 48864 is preparing a paper to be called "Detection strategies for optical lattice microscopy".
26. M.J. Booth, M.A.A. Neil, R. Juškaitis, and T. Wilson, "Adaptive aberration correction in a confocal microscope," *Proc. Natl. Acad. Sci. USA* **99**, 5788-5792 (2002).
27. J.D. Jackson, *Classical Electrodynamics*, second ed. (Wiley, New York, 1975), Secs. 9.8 and 9.9.
28. M. Born and E. Wolf, *Principles of Optics*, sixth (corrected) ed. (Pergamon, Oxford, 1980), Sec. 8.8.
29. M. Gu, *Principles of Three-Dimensional Imaging in Confocal Microscopes* (World Scientific, 1996).
30. S. Hell and E.H.K. Stelzer, "Properties of a 4Pi confocal fluorescence microscope," *J. Opt. Soc. Am. A* **9**, 2159-2166 (1992).
31. E. Wolf, "Electromagnetic diffraction in optical systems I. An integral representation of the image field," *Proc. R. Soc. London Ser. A* **253**, 349-357 (1959).
32. B. Richards and E. Wolf, "Electromagnetic diffraction in optical systems II. Structure of the image field in an aplanatic system," *Proc. R. Soc. London Ser. A* **253**, 358-379 (1959).
33. S.F. Gibson and F. Lanni, "Experimental test of an analytical model of aberration in an oil-immersion objective lens used in three-dimensional light microscopy," *J. Opt. Soc. Am.* **A8**, 1601-1613 (1991).
34. E.R. Dufresne and D.G. Grier, "Optical tweezer arrays and optical substrates created with diffractive optics," *Rev. Sci. Instrum.* **69**, 1974-1977 (1998).
35. G. Timp, *et al.*, "Using light as a lens for submicron, neutral-atom lithography," *Phys. Rev. Lett.* **69**, 1636-1639 (1992).
36. J.J. McClelland, R.E. Scholten, E.C. Palm, and R.J. Celotta, "Laser-focused atomic deposition", *Science* **262**, 877-880 (1993).
37. M. Mützel, *et al.*, "Atomic nanofabrication with complex light fields," *Appl. Phys. B* **77**, 1-9 (2003).
38. T. Tanaka, H.B. Sun, and S. Kawata, "Rapid sub-diffraction-limit laser micro/nanoprocessing in a threshold material system," *Appl. Phys. Lett.* **80**, 312-314 (2002).
39. X.L. Yang, L.Z. Cai, and Y.R. Wang, "Larger bandgaps of two-dimensional triangular photonic crystals fabricated by holographic lithography can be realized by recording geometry design," *Opt. Express* **12**, 5850-5856 (2004).
40. Perkin-Elmer UltraVIEW Live Cell Imager, <http://las.perkinelmer.com/content/livecellimaging/nipkow.asp>
41. M. Petráň, M. Hadravský, M.D. Egger, R. Galambos, "Tandem-scanning reflected-light microscope," *J. Opt. Soc. Am.* **58**, 661-664 (1968).
42. K. Bahlmann and S.W. Hell, "Electric field depolarization in high aperture focusing with emphasis on annular apertures," *J. Microsc.* **200**, 59-67 (2000).
43. E. Betzig, New Millennium Research, LLC, Okemos, MI 48864 is preparing a paper to be called "Optical lattice microscopy: implications for live cell and molecular imaging".

1. Introduction

The dynamic optical imaging of living cells has been greatly facilitated by the development of *in vivo* expressed fluorescent fusion proteins such as GFP [1], yet remains challenging due to the necessary division of the collected signal in a measurement volume of at least four dimensions representing space, time, and optional contrast parameters such as polarization, emission wavelength, or lifetime. To significantly improve the resolution in any of these dimensions without sacrificing resolution in the others, significantly greater signal must be collected in a noninvasive manner that minimizes photobleaching and related phototoxicity within the cell. In particular, efforts to improve volumetric spatial resolution by techniques such as evanescent wave [2,3] or nonlinear microscopy [4,5] must contend with a cubically decreasing number of fluorophores within the probe volume as the resolution improves, in

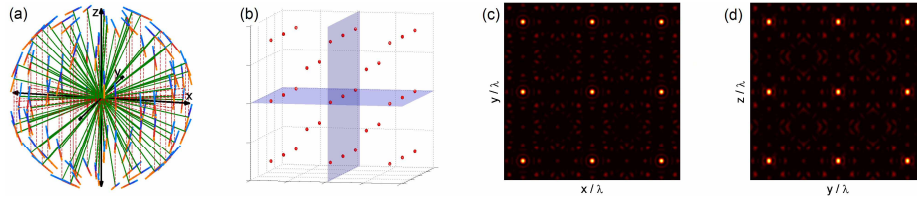


Fig. 1. A body-centered cubic sparse composite lattice of period $\sqrt{62}\lambda$ in $|\mathbf{e}(\mathbf{x})|^2$, with a basis that optimizes $|\mathbf{e}(\mathbf{x}) \cdot \hat{\mathbf{e}}_z|^2$ at the excitation maxima: (a) wavevectors \mathbf{k}_n (green) and electric field vectors \mathbf{e}_n (different colors for $t_q = t_o + 2\pi q/(8\omega)$, $q = 0 \dots 7$) for the 96 plane waves comprising the lattice; (b) isosurfaces of $0.5 \max(|\mathbf{e}(\mathbf{x})|^2)$ over $(10\lambda)^3$; (c, d) plots of $|\mathbf{e}(\mathbf{x})|^2$ over $(10\lambda)^2$ in the xy and yz planes shown in (b). Accompanying slide show (1.24 MB) presents plane wave properties and isosurfaces for 29 cubic lattices of differing periodicity, and includes six final frames indicating the fields \mathbf{e}_n that optimize different desired polarization states for a given lattice.

addition to their intrinsic efficiencies of signal generation. Consequently, extension of dynamic live cell imaging to the regime between macromolecules and organelles demands: simultaneous excitation and detection at many points throughout the imaged volume; confinement of the excitation to only these points; and efficient collection of luminescence.

Optical lattice excitation provides a means to achieve these goals. Such lattices are spatially periodic interference patterns resulting from the coherent superposition of a finite set of plane waves. Mathematical methods to find four wavevectors that define an optical lattice of any 3D Bravais symmetry have previously been developed [6,7]. Experimentally, optical lattices have been applied to microscopy in 1D or 2D form as single or paired standing waves for high resolution optical sectioning [8-10] or superresolution via structured illumination [11,12]. They have also been used to lithographically fabricate photonic crystals in 2D and 3D [13,14], with one aim being the creation of materials exhibiting a complete 3D photonic band gap [15]. Optical lattices are, however, perhaps most highly developed experimentally as periodic trapping potentials for ultracold atoms [16-18], where they can serve as idealized analogs of solid-state systems [19,20] and possibly as sites for individual atomic qubits in quantum computation [21,22].

In these applications, common problems have been that the lattice periodicity has been of the same order as the excitation wavelength λ , and that the intensity has varied on the same order as the periodicity. Thus, they have been too close packed to serve as three-dimensional arrays of individually resolvable, diffraction-limited excitation foci or trapping potentials. Expanding upon an existing crystallographic formalism [23], I recently addressed these issues by identifying two new classes of optical lattices, termed sparse and composite lattices, and determined the electric field \mathbf{e}_n and wavevector \mathbf{k}_n properties of their constituent plane waves necessary to create, at many periodicities both comparable to and large compared to λ , lattices of isolated excitation maxima of controllable polarization, each tightly confined in all directions, [24]. An example is shown in Fig. 1.

As seen in Fig. 1(a), the excitation of such lattices requires control over the wavevectors, electric fields, and phases of every member of a possibly large set of plane waves. In this paper, I consider theoretically the experimental means to achieve such control in a format consistent with efficient, individualized detection of the signal generated at each excitation maximum, and predict the effect of these means on the properties of the resulting lattice. The detection process itself will be considered in detail in a forthcoming paper [25].

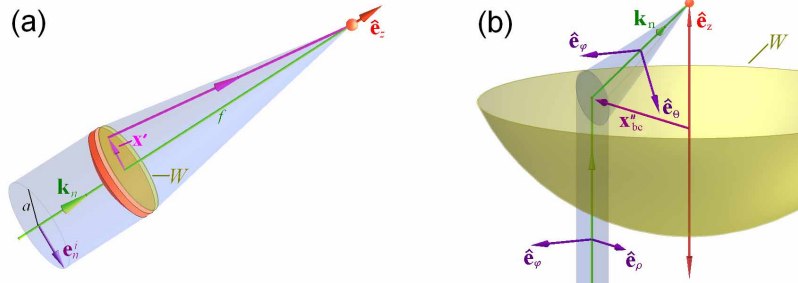


Fig. 2. Methods for the generation of confined beams comprising a bound lattice. (a) Uniform plane wave illumination along the optical axis \hat{e}_z of a lens of low numerical aperture ($a/f \ll 1$), oriented in the direction \mathbf{k}_n of the corresponding plane wave of the ideal lattice. (b) Localized, offset illumination in the rear pupil of a high numerical aperture microscope objective at the location $(\mathbf{x}''_{bc})_n$ yielding a convergent beam propagating along \mathbf{k}_n . A third method, illumination through an aperture in an opaque screen, is the $a/f \rightarrow 0$ limit of case (a).

2. Confined beams and bound lattices

An ideal lattice is infinite in extent. This is certainly true for an ideal optical lattice, since the ideal plane waves of which it is comprised are infinite in extent. Experimental realization demands that each such wave be replaced by a beam of finite width, introducing a continuous, albeit localized, distribution of wavevectors in place of each discrete vector \mathbf{k}_n . The first issue is therefore to determine the effect of this substitution on the properties of the lattice.

There are also practical reasons to consider *bound lattices* intentionally confined to *excitation zones* defined by the intersection of multiple beams of finite width. First, for nonlinear applications, absorption or scattering cross-sections are often sufficiently small to require excitation intensities accessible only with highly focused illumination. Second, confined excitation limits photobleaching and potential photodamage outside the field of view within biological specimens. Third, phase errors introduced by dynamically varying refractive index inhomogeneities within such specimens can be greatly reduced at a single lattice point with adaptive optical techniques [26], but will still accumulate with increasing distance from this point. Finally, lattices with well-defined boundaries may permit quantum simulation of surface effects in confined solid state systems (e.g., quantum dots), and can be used to control the number of particles contributing to an entangled quantum state.

Two methods for the production of confined beams are illumination through an aperture in an opaque screen and creation of a converging spherical wave with a lens. Both methods are either directly or indirectly relevant to scenarios for the experimental generation of bound lattices. However, the aperture problem can be considered as the $a/f \rightarrow 0$ limit of a lens of radius a and focal length f , so we initially concentrate on the latter, using the geometry shown in Fig. 2(a). Thus, an ideal plane wave $\mathbf{e}_n^i(\mathbf{x}, t) = \mathbf{e}_n \exp[i(kz - \omega t)]$, $\mathbf{e}_n \cdot \hat{e}_z = 0$ normally incident from $z < 0$ on a circular lens centered at $(x, y) = (0, 0)$ in an opaque screen at $z = 0$ creates a diffraction field $\mathbf{e}_n(\mathbf{x}, t)$ in the $z > 0$ half space that, for $ka \gg 1$, can be estimated using the generalized Kirchhoff integral [27]:

$$\mathbf{e}_n(\mathbf{x}, t) = -\frac{ik}{2\pi} \iint [\mathbf{e}_w(\mathbf{x}', t)]_n \frac{\exp(ik|\mathbf{x} - \mathbf{x}'|)}{|\mathbf{x} - \mathbf{x}'|} \left(1 + \frac{i}{k|\mathbf{x} - \mathbf{x}'|}\right) \frac{\hat{\mathbf{e}}_w \cdot (\mathbf{x} - \mathbf{x}')}{|\mathbf{x} - \mathbf{x}'|} d^2x', \quad (1)$$

where the integration is over all points \mathbf{x}' on the spherical wavefront W (yellow in Fig. 2(a)) of radius f and solid angle Ω subtended by the lens, $\hat{\mathbf{e}}_w$ is the unit vector normal to W , and $[\mathbf{e}_w(\mathbf{x}', t)]_n$ is given by the projection of the incident field $\mathbf{e}_n^i(\mathbf{x}, t)$ onto W .

First we consider the low numerical aperture (*na*) limit and use the paraxial approximation $a/f \equiv \sin \alpha \approx \alpha \ll 1$, since only a fairly narrow distribution of wavevectors is

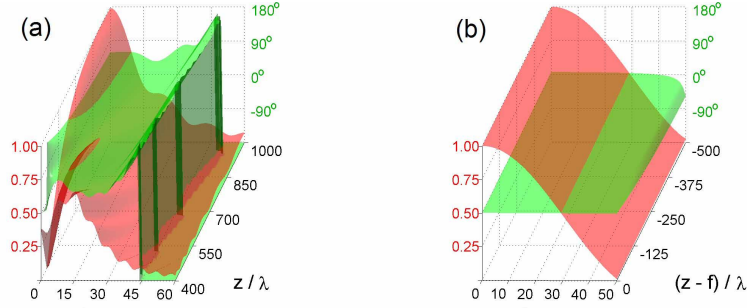


Fig. 3. Comparison of the amplitude (translucent red) and phase (translucent green) deviation from ideal plane wave behavior for the field diffracted from: a) a 30λ radius aperture and b) a lens of $a/f = 0.012$. Phase data is truncated after passing through $\pm 180^\circ$ for clarity. Animation accompanying (b) illustrates the evolution with increasing a/f (1.79 MB).

thereby introduced. Then, $[\mathbf{e}_w(\mathbf{x}', t)]_n \approx \mathbf{e}_n^i(x', y', 0, t)$. Further restricting our attention to field points \mathbf{x} satisfying $\sqrt{x^2 + y^2} \sim O(a)$ and $ka(a/z)^3 \ll 1$, Eq. (1) can then be expressed in cylindrical coordinates $\mathbf{x} \equiv (\rho \cos \theta, \rho \sin \theta, z)$, $\mathbf{x}' \equiv (\rho' \cos \theta', \rho' \sin \theta', z')$ as [28]:

$$\mathbf{e}_n(\mathbf{x}, t) \approx \left\{ -i \frac{a}{z} ka \exp\left(\frac{ik\rho^2}{2z}\right) (C(u, v) + iS(u, v)) \right\} \mathbf{e}_n \exp[i(kz - \omega t)] \quad (2a)$$

$$C(u, v) = \int_0^1 J_0(v\eta) \cos(u\eta^2/2) \eta d\eta \quad S(u, v) = \int_0^1 J_0(v\eta) \sin(u\eta^2/2) \eta d\eta \quad (3)$$

$$u(z) = \frac{a}{z} ka \quad v(\rho, z) = \frac{a}{z} k\rho \quad (4a)$$

Eqs. (2-4) are, to within the approximations already made, valid for both the aperture and lens scenarios. However, for the lens, it is convenient to recast the result in terms of the axial distance $z_f \equiv z - f$ from the focal point. For z_f satisfying $ka(a/f)(z_f/f)^2 \ll 1$, we find:

$$\mathbf{e}_n(\mathbf{x}, t) \approx \left\{ -i \frac{a}{f} ka \exp\left(\frac{ik\rho^2}{2f}\right) \exp(ikf) (C(u_l, v_l) - iS(u_l, v_l)) \right\} \mathbf{e}_n \exp[i(kz - \omega t)] \quad (\text{lens only}) \quad (2b)$$

$$u_l(z) = (a/f)^2 \cdot k(z - f) \quad v_l(x, y) = \frac{a}{f} k\rho \quad (\text{lens only}) \quad (4b)$$

Equations. (2a) and (2b) show that the diffracted field in each case has the form of an ideal plane wave traveling along the optical axis $\hat{\mathbf{e}}_z$, modified by a complex multiplier that determines the nature of the field confinement. As described elsewhere [28], the numerical evaluation of the integrals $C(u, v)$ and $S(u, v)$ in these multipliers is expedited by relating each to Lommel functions, a group of rapidly converging infinite series of Bessel functions.

Figure 3 compares the amplitude and phase of this complex confinement factor for an aperture of radius $a = 30\lambda$ to those of a lens with $a/f = 0.012$, expected to yield a beam waist at the focal point of similar size. Although either method provides the desired amplitude confinement, the lens approach is preferred, because it introduces negligible phase variation is over the entire central amplitude peak in the neighborhood of the focal point. Thus, throughout the excitation zone, the phase relationship between lens-confined beams of a bound lattice will remain nearly identical to the phase relationship between the corresponding plane waves of the associated ideal lattice, and lattice distortion will be minimized. Furthermore, whereas the diffraction field from the aperture diverges with increasing distance from its defining screen, the lens field converges to yield a higher intensity $I(0, v)/I_o = (2J_1(v)/v)^2$ and minimum width:

$$2\rho \approx 0.52\lambda/(a/f) \quad (5)$$

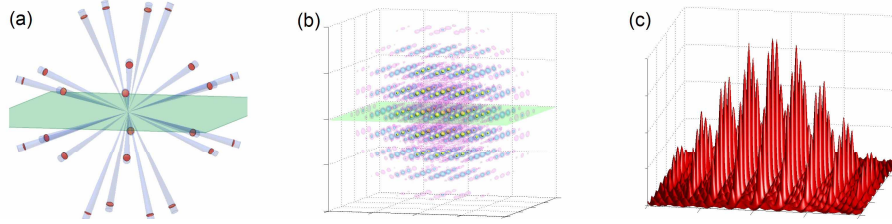


Fig. 4. (a) Creation of a simple cubic bound lattice (period $\sqrt{11}\lambda/2$ in $|\mathbf{e}(\mathbf{x})|^2$) with 24 individual low numerical aperture lenses (orange) focusing 24 convergent beams (translucent blue) to a common focal point. (b) Resultant lattice for $a/f = 0.08$, as seen via isosurfaces of 50% (yellow), 20% (aqua), and 10% (magenta) of $\max(|\mathbf{e}(\mathbf{x})|^2)$ over $(14.9\lambda)^3$. (c) Surface plot of $|\mathbf{e}(\mathbf{x})|^2$ across the green xy slice plane in (b). Corresponding animation (2.42 MB) illustrates the increase in lattice confinement with increasing a/f .

at the focal point dependent only on λ and the ratio a/f . Thus, extremely small excitation zones of width $2\rho \ll a$ can be created at arbitrarily large distances through appropriate choice of a and f . This simplifies the task of constructing an optical system to produce the large number of beams from diverse angles necessary for many lattices (e.g., Fig. 1(a)).

These results immediately suggest the lattice generation method of Fig. 4(a), wherein each plane wave of the ideal lattice is replaced by a low na circular lens, uniformly illuminated at normal incidence, with the lens axis aligned to the plane wave propagation vector \mathbf{k}_n , and having input polarization \mathbf{e}_n and phase set to achieve the desired basis field (i.e., the field that identically exists in every primitive cell of the ideal lattice) as described in Ref. [24]. Initially we consider only identical lenses sharing a common focal point, deferring more sophisticated geometries until later.

Figure 4(b) shows the bound lattice of total field $\mathbf{e}(\mathbf{x}, t)$ resulting when this arrangement is applied with lenses of $na = 0.08$ to the 24 plane waves of an ideal simple cubic lattice of period $\sqrt{11}\lambda/2$ in $|\mathbf{e}(\mathbf{x})|^2$. Maximally symmetric composite lattices of the cubic crystal group such as this, created with all plane waves consistent with the symmetry operations of the group, are of particular interest because they can produce isolated excitation maxima confined to near the diffraction limit in all directions when the basis is chosen as described in Ref. [24]. As expected for the wide range of ideal wavevector directions involved, the excitation zone is nearly spherically symmetric and, as indicated in the central slice in Fig. 4(c), exhibits an envelope full width at half maximum $2\rho \approx 9.6\lambda$ in rough agreement with Eq. (5). Furthermore, the widths of the *individual* excitation maxima and the background strength elsewhere within the excitation zone are nearly identical those of the ideal lattice, which is consistent with expectations based on the uniform phase observed in Fig 3(b).

The increase in confinement of the bound lattice with increasing na of the lenses is confirmed in the animation accompanying Fig. 4. Although beyond the limit of $a/f \ll 1$ assumed above, the na can be increased until the envelope width as given by Eq. (5) becomes smaller than the lattice spacing, at which point the single central lattice point dominates. In this limit, the total solid angle subtended by all N lenses, $\Omega_{tot} = N\Omega = 2\pi N(1 - \sqrt{1 - (a/f)^2})$, approaches 4π , or 2π if only the beams within one half space are included. Thus, excitation in single focus imaging systems such as the confocal [29] and 4π microscope [30] can be considered as continuum wavevector limits of bound lattice excitation.

3. Lattice excitation through high numerical aperture objectives

The experimental arrangement of Fig. 4(a) is unwieldy, requiring manipulation of the position and orientation of a large number of lenses, as well as separate optical elements to control the input polarization and phase of each beam. Furthermore, for most maximally symmetric

composite lattices, it leaves no large, unobstructed region for the inclusion of one or more high numerical aperture objective lenses to detect the resulting signal with high efficiency and spatial resolution. Whereas such an objective could be used by exciting only the subset lattice consisting of only those beams with ideal wavevector directions \mathbf{k}_n outside the solid angle occluded by the objective, confinement of the excitation maxima along the objective axis $\hat{\mathbf{e}}_z$ would be compromised, as in the confocal microscope, since the maximum spatial frequency along $\hat{\mathbf{e}}_z$ would be reduced from $2|\mathbf{k}_n \cdot \hat{\mathbf{e}}_z|_{\max}$ to approximately $|\mathbf{k}_n \cdot \hat{\mathbf{e}}_z|_{\max} - |\mathbf{k}_n \cdot \hat{\mathbf{e}}_z|_{\min}$.

An experimentally less complicated arrangement that optimizes both the excitation and detection resolution as well as the collection efficiency uses opposed high NA objectives both to deliver multiple beams to the excitation zone and to collect the resulting signal. This is analogous to the 4π microscope, except that illumination at specific, discrete points within the rear pupil of each objective creates a bound lattice with a plurality of excitation maxima, as opposed to the single, multi-lobed focus of the 4π microscope under uniform illumination.

To create by this method a convergent beam of effective cone half-angle $na \equiv a/f \ll 1$ propagating in the direction \mathbf{k}_n defined by a corresponding plane wave of a given ideal lattice, ray tracing indicates that the rear pupil (radius A) of an infinity corrected objective of numerical aperture NA , focal length F_o , and object space refractive index n should be illuminated at position:

$$(\mathbf{x}''_{bc})_n = -[(\mathbf{k}_n \cdot \hat{\mathbf{e}}_x)\hat{\mathbf{e}}_x + (\mathbf{k}_n \cdot \hat{\mathbf{e}}_y)\hat{\mathbf{e}}_y] \frac{F_o}{k} = -[(\mathbf{k}_n \cdot \hat{\mathbf{e}}_x)\hat{\mathbf{e}}_x + (\mathbf{k}_n \cdot \hat{\mathbf{e}}_y)\hat{\mathbf{e}}_y] \frac{n}{kNA} A \quad (6)$$

with an input beam of radius $b = na \cdot F_o$. The bound lattice resulting from the superposition of all such beams is then derived by determining, in the vicinity of the focal point of the objective, the diffracted field $\mathbf{e}_n(\mathbf{x}, t)$ arising from each.

To accomplish this, we follow the arguments of an oft-cited treatment of vector diffraction by a high NA lens [31,32]. For $kF_o \gg 1$ and points \mathbf{x} near the focal point such that $\mathbf{x} - \mathbf{x}' \approx F_o \hat{\mathbf{e}}_w$, the generalized Kirchoff diffraction integral of Eq. (1) simplifies to:

$$\mathbf{e}_n(\mathbf{x}, t) = -\frac{ik}{2\pi} \iint [\mathbf{e}_w(\mathbf{x}', t)]_n \frac{\exp(ik|\mathbf{x} - \mathbf{x}'|)}{|\mathbf{x} - \mathbf{x}'|} d^2x'. \quad (7)$$

The problem therefore reduces to two parts: finding the relationship of the input beam field $\mathbf{e}_n^i(\mathbf{x}'', t)$ at the plane of the rear pupil to the resulting field $[\mathbf{e}_w(\mathbf{x}', t)]_n$ on W , and evaluating the resulting integral.

In the low na paraxial analysis leading to Eqs. (2-4), the angles of refraction were sufficiently small that $[\mathbf{e}_w(\mathbf{x}', t)]_n$ could be approximated by directly mapping $\mathbf{e}_n^i(\mathbf{x}'', t)$ onto W . Now, however, because the solid angle $\Omega = 2\pi(1 - \sqrt{1 - (NA/n)^2})$ subtended by the objective is so large, there is significant modification of the input polarization and beam shape upon transmission, as shown in Fig. 2(b). Thus, an input ray at position \mathbf{x}'' in the rear pupil is transformed into a convergent ray propagating towards the focal point in the direction:

$$\begin{aligned} \hat{\mathbf{e}}_r(\mathbf{x}') &= [-(\hat{\mathbf{e}}_x \cdot \mathbf{x}'')\hat{\mathbf{e}}_x - (\hat{\mathbf{e}}_y \cdot \mathbf{x}'')\hat{\mathbf{e}}_y + \sqrt{F_o^2 - |\mathbf{x}''|^2}\hat{\mathbf{e}}_z] / F_o \\ &= [-(\hat{\mathbf{e}}_x \cdot \mathbf{x}')\hat{\mathbf{e}}_x - (\hat{\mathbf{e}}_y \cdot \mathbf{x}')\hat{\mathbf{e}}_y + \sqrt{F_o^2 - (\hat{\mathbf{e}}_x \cdot \mathbf{x}')^2 - (\hat{\mathbf{e}}_y \cdot \mathbf{x}')^2}\hat{\mathbf{e}}_z] / F_o \end{aligned} \quad (8)$$

Although the tangential component $\hat{\mathbf{e}}_\phi(\mathbf{x}'')$ associated with the input ray is unchanged in this process (i.e., $\hat{\mathbf{e}}_\phi(\mathbf{x}') = \hat{\mathbf{e}}_\phi(\mathbf{x}'')$), the radial component $\hat{\mathbf{e}}_\rho(\mathbf{x}'')$ is rotated by refraction in the objective to the direction $\hat{\mathbf{e}}_\theta(\mathbf{x}')$, where:

$$\hat{\mathbf{e}}_\theta(\mathbf{x}') = [\hat{\mathbf{e}}_r(\mathbf{x}') \times \hat{\mathbf{e}}_z] / \sqrt{1 - (\hat{\mathbf{e}}_r(\mathbf{x}') \cdot \hat{\mathbf{e}}_z)^2}, \quad \hat{\mathbf{e}}_\rho(\mathbf{x}'') = \hat{\mathbf{e}}_z \times \hat{\mathbf{e}}_\phi(\mathbf{x}'), \quad \hat{\mathbf{e}}_\theta(\mathbf{x}') = \hat{\mathbf{e}}_r(\mathbf{x}') \times \hat{\mathbf{e}}_\phi(\mathbf{x}') \quad (9)$$

Therefore, assuming the polarization \mathbf{e}_n^i is constant across the input beam, we find:

$$[\mathbf{e}_w(\mathbf{x}', t)]_n = \mathcal{H}(x', y') \psi_n(x', y') [(\hat{\mathbf{e}}_\rho(\mathbf{x}'') \cdot \mathbf{e}_n^i)\hat{\mathbf{e}}_\theta(\mathbf{x}') + (\hat{\mathbf{e}}_\phi(\mathbf{x}'') \cdot \mathbf{e}_n^i)\hat{\mathbf{e}}_\phi(\mathbf{x}')] \quad (10)$$

where $\psi_n(x', y') = \psi_n(\mathbf{x}'')$ gives the variation in the amplitude of the input beam across the rear pupil (i.e., $\mathbf{e}_n^i(\mathbf{x}'', t) = \psi_n(\mathbf{x}'')\mathbf{e}_n^i \exp(-i\omega t)$), and $\chi(x', y')$ describes how this amplitude is transformed upon projection onto W .

As seen in Fig. 2(b), the beam energy $dE_n(\mathbf{x}'') \propto |\mathbf{e}_n^i(\mathbf{x}'')|^2 dx'' dy''$ in area $dx'' dy''$ within the rear pupil maps onto the curved element of W at $\mathbf{x}' = \mathbf{x}'' - \sqrt{F_o^2 - |\mathbf{x}''|^2} \frac{\hat{\mathbf{e}}_z}{F_o}$ with area $dx' dy' / (\hat{\mathbf{e}}_r(\mathbf{x}') \cdot \hat{\mathbf{e}}_z)$. Hence, energy conservation demands $\chi(x', y') = \sqrt{\hat{\mathbf{e}}_r(\mathbf{x}') \cdot \hat{\mathbf{e}}_z}$. To find \mathbf{e}_n^i , we also see in Fig. 2(b) that the central input ray at $(\mathbf{x}''_{bc})_n$ of Eq. (6) produces the central output ray along \mathbf{k}_n having a field $[\mathbf{e}_w(\mathbf{x}', t)]_n$ as given by Eq. (10) with $\hat{\mathbf{e}}_r(\mathbf{x}') = \mathbf{k}_n / k$ in Eq. (9). This field must match the polarization \mathbf{e}_n of the corresponding plane wave of the ideal lattice to achieve the desired basis. Therefore, working backwards through the objective:

$$\mathbf{e}_n^i = [(\hat{\mathbf{e}}_\theta)_n \cdot \mathbf{e}_n](\hat{\mathbf{e}}_\rho)_n + [(\hat{\mathbf{e}}_\phi)_n \cdot \mathbf{e}_n](\hat{\mathbf{e}}_\phi)_n \quad (11)$$

where $(\hat{\mathbf{e}}_\theta)_n = \hat{\mathbf{e}}_\theta((\mathbf{x}''_{bc})_n)$, $(\hat{\mathbf{e}}_\rho)_n = \hat{\mathbf{e}}_\rho((\mathbf{x}''_{bc})_n)$, and $(\hat{\mathbf{e}}_\phi)_n = \hat{\mathbf{e}}_\phi((\mathbf{x}''_{bc})_n)$. Combining these results with Eqs. (8-10), we finally arrive at the field of the convergent beam in the vicinity of the focal point of the objective:

$$\begin{aligned} \mathbf{e}_n(\mathbf{x}, t) = & -\frac{ik}{2\pi} \int_{-A}^A \int_{-A}^A \Theta\left(\frac{\sqrt{x'^2 + y'^2}}{A}\right) \left\{ \left[(\zeta(x', y')x'^2 + y'^2)(\hat{\mathbf{e}}_x \cdot \mathbf{e}_n^i) + (\zeta(x', y') - 1)x'y'(\hat{\mathbf{e}}_y \cdot \mathbf{e}_n^i) \right] \hat{\mathbf{e}}_x \right. \\ & + \left[(\zeta(x', y') - 1)x'y'(\hat{\mathbf{e}}_x \cdot \mathbf{e}_n^i) + (x'^2 + \zeta(x', y')y'^2)(\hat{\mathbf{e}}_y \cdot \mathbf{e}_n^i) \right] \hat{\mathbf{e}}_y \\ & \left. + (\sqrt{x'^2 + y'^2}) \left[x'(\hat{\mathbf{e}}_x \cdot \mathbf{e}_n^i) + y'(\hat{\mathbf{e}}_y \cdot \mathbf{e}_n^i) \right] \hat{\mathbf{e}}_z \right\} \frac{\sqrt{\hat{\mathbf{e}}_r(\mathbf{x}') \cdot \hat{\mathbf{e}}_z}}{x'^2 + y'^2} \psi_n(x', y') \frac{\exp(ik|\mathbf{x} - \mathbf{x}'|)}{|\mathbf{x} - \mathbf{x}'|} dx' dy' \end{aligned} \quad (12)$$

where $\zeta(x', y') = \sqrt{F_o^2 - x'^2 - y'^2} / F_o$, and $\Theta(x) = 1$ for $x \leq 1$, 0 otherwise.

In the special case where the input beam uniformly illuminates the entire rear pupil with a linearly polarized plane wave (i.e., $\psi_n(\mathbf{x}'') = e_o$), Eq. (12) yields the single excitation maximum at the focal point of the confocal microscope, and described in terms of three integrals I_0, I_1, I_2 , each over the single spherical coordinate variable θ' , in Ref. [32]. However, for the case of localized ($b < A$) offset ($(\mathbf{x}''_{bc})_n \neq 0$) illumination considered here, the double integral in Eq. (12) must be evaluated numerically, using a mesh of $|\Delta \mathbf{x}| \ll F_o / (|\mathbf{x}|_{\max} / \lambda)$ to accurately estimate the phase term $\exp(ik|\mathbf{x} - \mathbf{x}'|)$.

There still remains the issue of finding an experimentally realizable form of the complex input beam confinement factor $\psi_n(\mathbf{x}'')$ that leads to a lattice bound to an excitation zone of the desired size, shape, and edge sharpness, yet that closely approximates the ideal lattice therein. Four possibilities are considered across the columns of Fig. 5, and evaluated for the particular case of a maximally symmetric composite simple cubic lattice of period $\sqrt{3}\lambda/2$ in $|\mathbf{e}(\mathbf{x})|^2$, chosen because all eight constituent wavevectors $\mathbf{k}_n = k(\pm \hat{\mathbf{e}}_x \pm \hat{\mathbf{e}}_y \pm \hat{\mathbf{e}}_z) / \sqrt{3}$ lie within the illumination cones of opposed $NA = 1.2$ water immersion objectives.

Column 1 of Fig. 5 considers the case of input beams created with a mask containing circular apertures. $\psi_n(\mathbf{x}'')$ is then given by the confinement factor in Eq. 2a. To highlight possible distortions of each beam on passage through the objective, an aperture radius $b = 0.055A$, expected to yield an excitation zone of width $2\rho \sim 10\lambda$, is used. The mask is placed a distance $z_{\text{mask}} = 2 \cdot 10^4 \lambda \ll b^2 / \lambda$ from the rear pupil plane sufficiently remote to be outside the path of the collected signal, yet sufficiently near that the wavevector spread $\Delta k / k \sim O(\lambda / b)$ introduced by the aperture does not significantly influence the input beam field over the majority of its diameter at the rear pupil plane (i.e., so that $(\Delta k / k)z \ll a$).

With these parameters, the amplitude $|\psi_n(\mathbf{x}'')|$ and phase $\arg[\psi_n(\mathbf{x}'')]$ plots in rows 1 and 2, respectively, of the particular input beam centered at $(\mathbf{x}''_{bc})_n = 0.64(\hat{\mathbf{e}}_x + \hat{\mathbf{e}}_y) / A$ demonstrate that the beam remains largely confined to the original aperture diameter at the pupil plane, with relatively uniform phase within this diameter. Consequently, the electric field energy density $|\mathbf{e}_n(\mathbf{x}_\perp)|^2$ across the focal point of the resulting convergent beam is confined to approximately the expected width (row 3) in the $\hat{\mathbf{e}}_\phi$ direction, and the phase

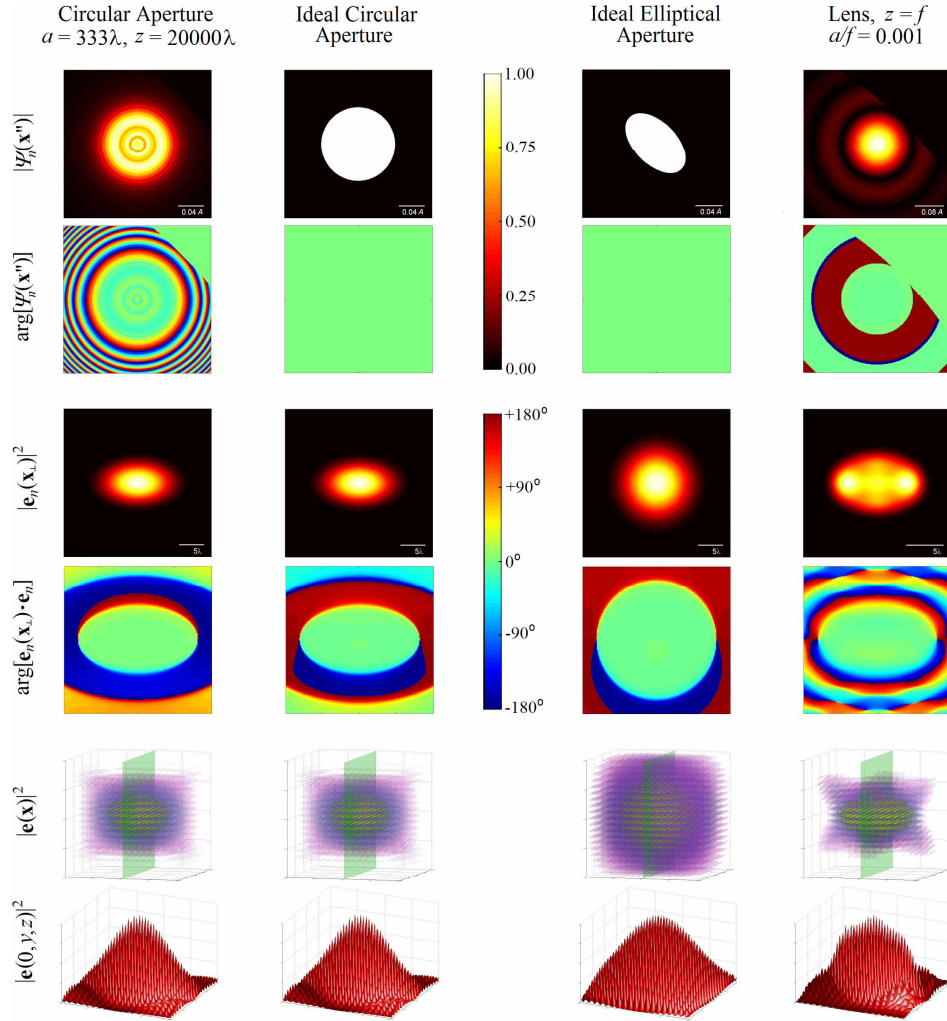


Fig. 5. Comparison of four different input beam models (as characterized by the confinement factor $\psi_n(\mathbf{x}'')$) for the generation of convergent beams $\mathbf{e}_n(\mathbf{x}, t)$ through a high NA objective, as applied to a specific beam $\mathbf{k}_n = -k(\hat{\mathbf{e}}_x + \hat{\mathbf{e}}_y + \hat{\mathbf{e}}_z)/\sqrt{3}$ of a simple cubic lattice of period $\sqrt{3}\lambda/2$. Also compared are the resulting excitation zones of $|\mathbf{e}(\mathbf{x})|^2$ when each model is applied to all beams of the lattice.

$\arg[\mathbf{e}_n(\mathbf{x}_\perp) \cdot \mathbf{e}_n]$ of its desired electric field component exhibits the uniformity (row 4) across this width necessary for the creation of a bound lattice of minimal distortion (rows 5, 6).

These results, obtained with a realistic input field, can be compared to those for an idealized circular field having infinite amplitude sharpness (column 2, row 1) and constant phase (column 2, row 2). The close similarities between the resulting convergent beams in both amplitude (row 3) and phase (row 4) indicate that the latter, simpler model can be used whenever $z_{\text{mask}} \ll b^2/\lambda$. Both models also indicate an elliptical compression of the convergent beam in the $\hat{\mathbf{e}}_\theta$ direction (row 3) that distorts the shape of the final excitation zone (row 5). This occurs, as shown in Fig. 2(b), when the circular input beam is projected onto the curved surface W , creating a convergent beam initially *stretched* by a factor $k/(\mathbf{k}_n \cdot \hat{\mathbf{e}}_z)$ along $\hat{\mathbf{e}}_\theta$ based on its location $(\mathbf{x}''_{bc})_n$ in the rear pupil. The effective na of the beam is then $kb/(F_0 \mathbf{k}_n \cdot \hat{\mathbf{e}}_z)$ in this direction rather than b/F_0 , creating an elliptical beam waist at the focus reduced by $(\mathbf{k}_n \cdot \hat{\mathbf{e}}_z)/k$ along $\hat{\mathbf{e}}_\theta$ according to Eq. (5).

It is possible to compensate for this effect, as shown in column 3 of Fig. 5, by using an elliptical aperture, reduced by a factor of $(\mathbf{k}_n \cdot \hat{\mathbf{e}}_z)/k$ in the $\hat{\mathbf{e}}_\rho$ direction. Based on the above results an ideal elliptical input field model can be used (column 3, rows 1 and 2), provided $z_{mask} \ll [b(\mathbf{k}_n \cdot \hat{\mathbf{e}}_z)/k]^2/\lambda$. The resulting convergent beam exhibits the expected circular waist with good phase uniformity (rows 3, 4), and a spherical excitation zone (rows 5, 6).

As the desired excitation zone width 2ρ increases, the required aperture diameter or major axis width $2b \approx 0.52\lambda F_o/\rho$ becomes so small that the mask can no longer be placed outside the path of the collected signal while still satisfying $z_{mask} \ll b^2/\lambda$ as required to achieve good amplitude confinement and phase uniformity of the input and convergent beams. For fluorescence microscopy, a patterned dichroic mirror or dichroic mask in the signal path could be used instead. More generally, a low na lens, such as in Figs. 3(b), could be used to define each input beam and placed at a large distance from the rear pupil by increasing the focal length f and radius a in tandem. An excitation zone of width 2ρ should then result for an input beam diameter $2b \approx 0.52n\lambda f/a$, or $a/f = na = n\rho/F_o$. The case of $2\rho \approx 10\lambda$, yielding $a/f \approx 0.001$ for $n = 1.33$ and $F_o = 6.6 \times 10^3 \lambda$, is considered in column 4 of Fig. 5.

In this column, the amplitude $|\psi_n(\mathbf{x}'')|$ (row 1) and excitation zone (row 5) are indeed confined to the expected dimensions. However, even when the lens is placed with its focal point coincident with the rear pupil plane, so that $\arg[\psi_n(\mathbf{x}'')]$ (row 2) is constant over the central maximum, there remains enough beam energy of opposite phase in the first annulus of $|\psi_n(\mathbf{x}'')|$ that the convergent beam (row 3,4) is distorted, affecting both the excitation zone symmetry and lattice quality near its periphery (row 6). Therefore, the aperture method of defining the input beams is preferred whenever the condition $z_{mask} \ll b^2/\lambda$ can be met.

4. Tailoring the lattice to the optical geometry

Besides greater experimental simplicity, the delivery of constituent beams of a bound lattice to the excitation zone *via* precision, high NA apochromatic microscope objectives permits compensation for chromatic and spherical aberration. The former is necessary to achieve diffraction-limited performance and correctable dispersion with ultrafast, pulsed excitation, and the latter is required to achieve the amplitude and phase characteristics for each convergent beam predicted by Eq. (12) and seen in Fig. 5. Cover glass correction can also be used when illuminating substrate mounted specimens to compensate for the rapidly varying optical path across oblique convergent beams of moderate na .

Unfortunately, however, opposed water immersion objectives cover a total solid angle ($\Omega = 4\pi(1 - \sqrt{1 - (NA/n)^2}) \approx 2.28\pi$ steradians at $NA = 1.2$) insufficient to encompass all beams of most maximally symmetric composite lattices, particularly those of the cubic crystal group that can produce particularly symmetric, well-confined excitation maxima. One solution, as shown in Fig. 6(a), is simply to omit those beams (translucent gold) whose ideal wavevectors \mathbf{k}_n fall outside the illumination cones (translucent green) defined by the objectives. However, the transverse confinement $[(\mathbf{k}_m - \mathbf{k}_n) \cdot \hat{\mathbf{e}}_{x,y}]_{\max}$ of the maxima (Fig. 6(b)) and their contrast with respect to the remainder of each primitive cell (Figs. 6(c),(d)) is thereby reduced, while the weighting of spatial frequencies $(\mathbf{k}_m - \mathbf{k}_n) \cdot \hat{\mathbf{e}}_z$ along the optical axis is increased. This leads to a multi-lobed excitation profile (Figs. 6(b),(d)) similar to the 4π microscope, and introduces uncertainty as to from which lobe a given signal photon originated.

Of course, the lattice need not necessarily be oriented with its c -axis aligned to the objective axis $\hat{\mathbf{e}}_z$, and hence the number of wavevectors \mathbf{k}_n that lie within the objective illumination cones can often be increased by choosing an appropriate orientation. With the omission of fewer beams, the transverse confinement of the maxima and their contrast is thereby improved. Alternatively, the number of beams within the illumination cones can be increased by changing the geometric properties of the ideal lattice and hence the distribution of its constituent wavevectors. Thus, all the wavevectors of any 2D lattice oriented with its

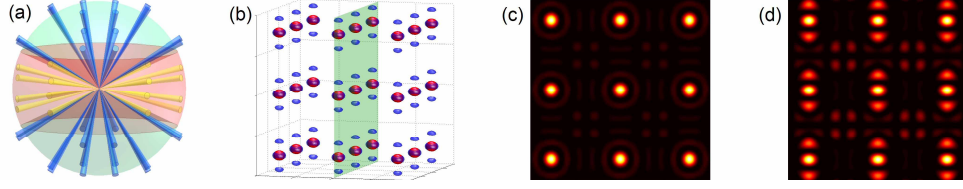


Fig. 6. (a) Geometric arrangement of the beams comprising a maximally symmetric simple cubic bound lattice of period $\sqrt{35}\lambda/2$ in $|\mathbf{e}(\mathbf{x})|^2$ with c -axis $\parallel \hat{\mathbf{e}}_z$, shown in relation to the illumination cones (translucent green) of opposed objectives ($NA = 1.2, n = 1.33$). (b) Isosurfaces of $0.4 \max[|\mathbf{e}(\mathbf{x})|^2]$ for both the maximally symmetric lattice (opaque red) comprised of all 48 beams, and the subset lattice (translucent blue) comprised of only the 32 beams (blue in (a)) internal to the objectives. The basis is chosen to optimize $|\mathbf{e}(\mathbf{x}) \cdot \hat{\mathbf{e}}_x|^2$ at the excitation maxima. (c,d) Plots of $|\mathbf{e}(\mathbf{x})|^2$ for the maximally symmetric lattice and subset lattice, respectively, in the yz -plane in (b).

invariant axis along $\hat{\mathbf{e}}_z$ can be included by reducing their common cone angle $\theta_{2D} = \cos^{-1}(\mathbf{k}_n \cdot \hat{\mathbf{e}}_z / k)$ to fall within the maximum illumination angle $\theta_{\max} = \sin^{-1}(NA/n)$ of the objective. Similarly, by decreasing the unit cell aspect ratio c/a of any 3D lattice having symmetry (e.g., tetragonal) permitting such adjustment and oriented with c -axis $\parallel \hat{\mathbf{e}}_z$, the wavevector distribution can be altered to produce the highest possible transverse spatial frequency $2kNA/n$ and resulting maxima confinement for the given objectives.

5. Hybrid excitation

Despite these methods, transverse resolution and excitation contrast is unavoidably compromised, and multi-lobed excitation profiles necessarily introduced, when the wavevector distribution is restricted to the illumination cones of opposed objectives. Thus, to achieve optimal bound lattice excitation, it is necessary to create convergent beams propagating in all directions defined by the wavevectors of the corresponding ideal maximally symmetric composite lattice. This limit can be approached using *hybrid excitation*, wherein a combination of illumination internal and external to the objectives is used.

Figure 7 illustrates this process for a maximally symmetric body-centered cubic lattice of period $\sqrt{5}\lambda$ in $|\mathbf{e}(\mathbf{x})|^2$, consisting of 24 plane waves. Eight input beams are introduced at the rear pupil of each of two opposed $NA = 1.2$ water immersion objectives (Fig. 7(a)), and elliptically compressed by $(\mathbf{k}_n \cdot \hat{\mathbf{e}}_z)/k$ along $\hat{\mathbf{e}}_\rho$ to produce a spherical excitation zone. The extent of the beams is limited to yield an effective na for the corresponding convergent beams of 0.02, insuring that the beams nearest the periphery fit entirely within the rear pupil (Fig. 7(b)). The polarization \mathbf{e}_n^i of each beam is set according to Eq. (11) to achieve a basis that optimizes $|\mathbf{e}(\mathbf{x}) \cdot \hat{\mathbf{e}}_x|$ at the excitation maxima.

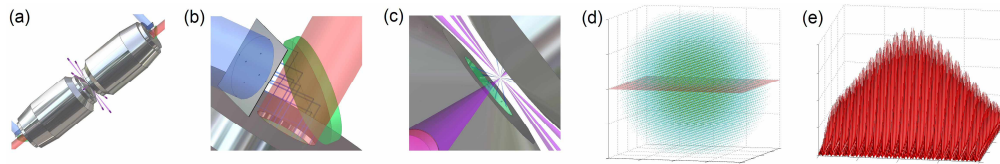


Fig. 7. Hybrid excitation of a bound lattice: a) Overall view, showing opposed objectives; b) Expanded view near one rear pupil, showing input beams (blue) defined with an aperture mask, and an output signal beam (red) isolated with a dichroic mirror (green); c) Expanded view between the objectives, showing 8 convergent beams (blue) generated internal to each objective as well 8 beams (purple) generated externally with individual low na lenses; d) Resulting lattice over $(\pm 21\lambda)^3$, exhibiting a spherical excitation zone, as seen via isosurfaces of 0.5 (yellow) and 0.2 (aqua) of $\max[|\mathbf{e}(\mathbf{x})|^2]$; e) Surface plot of $|\mathbf{e}(\mathbf{x})|^2$ through the xy slice plane (red) in (d).

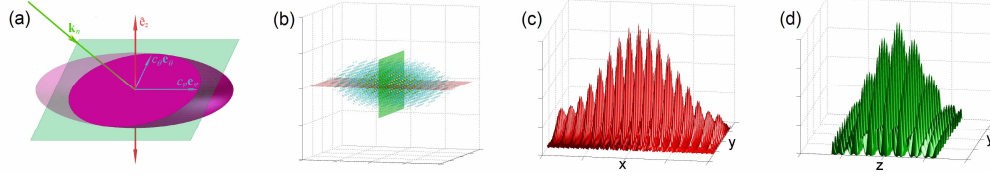


Fig. 8. Shaping the excitation zone by shaping the cross-section of each constituent beam: (a) Geometry and relevant parameters; (b) Ellipsoidal excitation zone over $(\pm 12\lambda)^3$ for a hybrid excited, maximally symmetric BCC lattice of period $\sqrt{2}\lambda$ in $|\mathbf{e}(\mathbf{x})|^2$, comprised of twelve shaped beams; (c,d) Surface plots of $|\mathbf{e}(\mathbf{x})|^2$ through the xy (red) and yz (green) slice planes, respectively, in (b). Accompanying movie (1.05 MB) illustrates the shapes of the four input beams at the rear pupil of one objective ($NA = 1.2$) that yield various ellipsoidal excitation zones as shown when superimposed with all other appropriately shaped beams of the lattice.

Despite the short working distances of the objectives, a small secondary illumination region exists between them. It is here that the remaining eight beams of the maximally symmetric lattice are introduced, using individual circular lenses also of $na = 0.02$, each illuminated at the polarization \mathbf{e}_n of the corresponding ideal plane wave to achieve the desired basis, and each confocal with the common focal point of the objectives (Fig. 7(c)).

The hybrid bound lattice resulting from the superposition of both the internal and external beams, the former calculated *via* Eq. (12) and the latter *via* Eq. (2b), is shown in Figs. 7(d),(e). The excitation zone is indeed spherically symmetric, near the expected diameter, and closely approximates the ideal lattice therein.

Unfortunately, even with hybrid excitation, many maximally symmetric composite lattices will include a few beams that fall within the occlusion regions defined by the working distances and nosepiece geometries of the objectives. The number of such beams can often be reduced by rotating the lattice or changing the unit cell dimensions as discussed above, or possibly by cutting slots in each nosepiece at the locations of specific external beams.

For imaging cultured cells, another challenge is to compensate for reflection, displacement, and aberration to the external beams [33], which by necessity intersect the mounting substrate at exceptionally oblique angles. Although aberrations can be reduced by decreasing the na of the external beams or by phase compensating with a spatial light modulator (SLM), a simpler prescription may be to dispense with the substrate and immobilize the cell instead with a patch clamp pipette or a single or multiple point [34] optical trap, the latter possibly created with a second lattice at wavelength λ_{trap} .

6. Shaping the excitation zone

The ideal excitation zone would cover the region of interest with a uniform envelope having a boundary of infinite sharpness, so that the excitation energy would be optimally concentrated, photobleaching would be minimized, and all excitation maxima would be of equal strength. However, in the above examples, the zone is constrained to a spherical shape having a boundary sharpness of the same order as its diameter, since the common na of the convergent beams is left as the only controllable parameter. To achieve greater control over the shape, uniformity, and sharpness of the zone, similar control must be exerted over the properties of the convergent beams and how they intersect to define the zone.

One approach is to tailor the shape of each convergent beam such that its cross-section at its beam waist matches the desired cross-section of the excitation zone perpendicular to the propagation direction \mathbf{k}_n (Fig. 8(a)). For every internal beam, the dimensions of the input beam at the rear pupil of the objective in the $(\hat{\mathbf{e}}_\phi)_n = \hat{\mathbf{e}}_\phi((\mathbf{x}''_{bc})_n)$ and $(\hat{\mathbf{e}}_\rho)_n = \hat{\mathbf{e}}_\rho((\mathbf{x}''_{bc})_n)$ directions of Eq. (9) are then determined by applying Eq. (5) to the cross-sectional widths c_ϕ ,

c_θ of the zone in the $(\hat{\mathbf{e}}_\phi)_n$ and $(\hat{\mathbf{e}}_\theta)_n = \hat{\mathbf{e}}_\theta((\mathbf{x}''_{bc})_n)$ directions, respectively. An additional compression factor of $(\mathbf{k}_n \cdot \hat{\mathbf{e}}_z)/k$ is applied along $(\hat{\mathbf{e}}_\rho)_n$ to compensate for the ellipticity effect seen in Figs. 2(b) and 5. For external beams, the effective lens na in directions orthogonal to \mathbf{k}_n is set inversely to the cross-sectional dimensions of the zone as per Eq. (5).

Application of this approach to an ellipsoidal excitation zone of desired aspect ratio 2:6:1 along the principal axes is shown in Fig 8(b). The observed ratio of $\sim 1.5:2.5:1$ reflects the $[\sin(u_l z_l)/u_l z_l]^2$ axial dependence of the intensity near the focus of each convergent beam, which serves to further restrict the excitation zone for beams of sufficiently high na . Nevertheless, the xy and yz plots in Figs. 8(c) and 8(d), respectively, indicate that the lattice properties are well preserved within this envelope.

A second approach is to tailor the shape and uniformity of the zone by altering the relative positions of the convergent beam waists. However, at points where their mutual overlap becomes too low, the relative contributions of the constituent wavevectors can become too uneven, adversely affecting the confinement of the individual lattice excitation maxima and their background contrast.

Neither of these approaches directly affects the sharpness of the zone boundary relative to its extent, since both are dependent upon the na of the convergent beams. Independent control of these parameters can be achieved, however, by constructing a composite excitation zone consisting of Z smaller, overlapping excitation sub-zones. The boundary sharpness is then dictated by the width of each sub-zone, and the shape of the overall zone is determined by their spatial distribution. The positions as well as the phases of the N beams comprising each sub-zone should be chosen relative to all others to create a uniform field of lattice excitation maxima within the composite zone.

The first step in the creation of such composite zones is to determine how to center each sub-zone at a position other than the common focal point of the objectives. This requires translating in unison the convergent beams comprising each sub-zone. For external beams, standard paraxial theory predicts the waist of a given convergent beam can be translated transversely by Δx_t in the vicinity of the focal point by illuminating the lens at an angle $\alpha_t = \Delta x_t / f$ to the lens axis. Axial translation by Δz is then accomplished by illuminating the lens with a spherical wavefront of curvature $s = f^2 / \Delta z$ rather than a planar one.

This suggests that we consider the possibility of translating the beam waists of internally generated beams by similar means. Thus, the rear pupil of the objective is again illuminated with an offset, localized input beam centered at $(\mathbf{x}''_{bc})_n$ and having a complex confinement factor $\psi_n(\mathbf{x}'')$. However, the beam is now considered to originate from a point source at position $(\mathbf{x}''_s)_n$ beyond the rear pupil plane prior to its confinement by means such in Fig. 5, introducing an additional phase term $\Phi_n(x', y') = k[x'\hat{\mathbf{e}}_x + y'\hat{\mathbf{e}}_y - [(\mathbf{x}''_s)_n - (\mathbf{x}''_{bc})_n]]$ characteristic of an offset spherical wave in Eq. (7):

$$\mathbf{e}_n(\mathbf{x}, t) = -\frac{ik}{2\pi} \iint \exp[i\Phi_n(x', y')] [\mathbf{e}_w(\mathbf{x}', t)]_n \frac{\exp(ik|\mathbf{x} - \mathbf{x}'|)}{|\mathbf{x} - \mathbf{x}'|} d^2x' \quad (13)$$

If the input beam major axis half-length satisfies $b \ll \sqrt{s^3 \lambda / F_o^2}$, $s = |(\mathbf{x}''_s)_n - (\mathbf{x}''_{bc})_n|$, then:

$$\begin{aligned} \Phi_n(x', y') &= k\sqrt{s^2 + (x'_\phi)^2 + (x'_\rho + \rho_{bc})^2} - 2x''_\phi x'_\phi - 2(x''_\rho + \rho_{bc})(x'_\rho + \rho_{bc}) \\ &\approx ks - \frac{kx''_\phi}{s} \mathcal{E}'_\phi - \frac{k(x''_\rho + \rho_{bc})}{s} \mathcal{E}'_\rho + \frac{k}{2s} [(\mathcal{E}'_\phi)^2 + (\mathcal{E}'_\rho)^2] \end{aligned} \quad (14)$$

where $x'_\phi \equiv \mathbf{x}' \cdot (\hat{\mathbf{e}}_\phi)_n$, $x'_\rho \equiv \mathbf{x}' \cdot (\hat{\mathbf{e}}_\rho)_n$, $x''_\phi \equiv (\mathbf{x}''_s)_n \cdot (\hat{\mathbf{e}}_\phi)_n$, $x''_\rho \equiv (\mathbf{x}''_s)_n \cdot (\hat{\mathbf{e}}_\rho)_n$, $(\mathbf{x}''_{bc})_n = -\rho_{bc}(\hat{\mathbf{e}}_\rho)_n$, $\mathcal{E}'_\phi \equiv [\mathbf{x}' - (\mathbf{x}''_{bc})_n] \cdot (\hat{\mathbf{e}}_\phi)_n$, and $\mathcal{E}'_\rho \equiv [\mathbf{x}' - (\mathbf{x}''_{bc})_n] \cdot (\hat{\mathbf{e}}_\rho)_n$. However, for points \mathbf{x} sufficiently close to the objective focal point to satisfy $|\mathbf{x}| \ll \sqrt{2F_o \lambda}$, the original phase term $k|\mathbf{x} - \mathbf{x}'| \approx k|\mathbf{x}'| - k\mathbf{x} \cdot \mathbf{x}'/|\mathbf{x}'|$ can be expressed as:

$$k|\mathbf{x} - \mathbf{x}'| \approx kF_o + kx_k - \frac{kx_\phi}{F_o} \mathcal{E}'_\phi + \frac{kx_\theta}{F_o \cos \Upsilon} \mathcal{E}'_\rho - \frac{k(x_\theta \tan \Upsilon + x_k)}{2F_o^2} [(\mathcal{E}'_\phi)^2 + (\mathcal{E}'_\rho)^2] \quad (15)$$

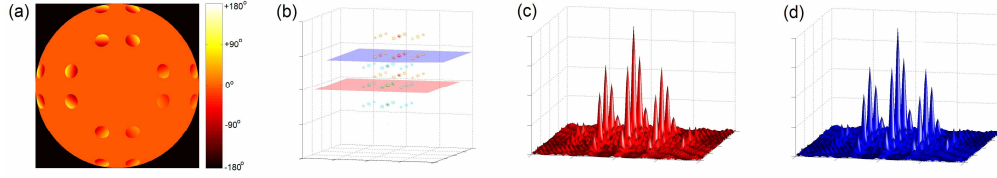


Fig. 9. Translating the excitation zone by phase-steering each constituent beam to a common offset point: a) Phase variation across the 16 input beams at the rear pupil of one of the objectives ($NA = 1.2$), as required to produce an offset of $\Delta \mathbf{x} = (3\hat{\mathbf{e}}_x + 4\hat{\mathbf{e}}_y + 5\hat{\mathbf{e}}_z)\lambda$; b) Isosurfaces of $0.5 \max[|\mathbf{e}(\mathbf{x})|^2]$ and $0.2 \max[|\mathbf{e}(\mathbf{x})|^2]$ for the original, centered bound lattice (yellow and aqua, respectively) and the resulting offset bound lattice (magenta and orange, respectively); c,d) Surface plots of $|\mathbf{e}(\mathbf{x})|^2$ for the centered and offset lattices, respectively, through the xy slice planes in (b). Accompanying animation (1.0 MB) shows the changes in phase variation across each input beam at the rear pupil of one objective as the lattice is translated to different points.

where $x_\phi \equiv \mathbf{x} \cdot (\hat{\mathbf{e}}_\phi)_n$, $x_\theta \equiv \mathbf{x} \cdot (\hat{\mathbf{e}}_\theta)_n$, $x_k \equiv \mathbf{x} \cdot \mathbf{k}_n / k$, and $\cos \Upsilon = \mathbf{k}_n \cdot \hat{\mathbf{e}}_z / k$. Thus, combining Eqs. (13-15) and comparing the result to Eq. (7), we see that Eq. (13) leads to a convergent beam field $\mathbf{e}_n(\mathbf{x}, t)$ identical to that in Eq. (12), except offset by a distance $\Delta \mathbf{x}$ from the focal point of the objective, when the spherical wave generating the input beam is of radius:

$$s = F_o^2 \cos \Upsilon / \Delta z \quad (16)$$

at $(\mathbf{x}''_{bc})_n$ and centered beyond the rear pupil of the objective at:

$$(\mathbf{x}''_s)_n = (\mathbf{x}''_{bc})_n - [\Delta x_\phi \cos \Upsilon (\hat{\mathbf{e}}_\phi)_n - \Delta x_\theta (\hat{\mathbf{e}}_\theta)_n + \sqrt{(F_o^2 - \Delta x_\phi^2) \cos^2 \Upsilon - \Delta x_\theta^2} \hat{\mathbf{e}}_z] F_o / \Delta z \quad (17)$$

where $\Delta x_\phi \equiv \Delta \mathbf{x} \cdot \hat{\mathbf{e}}_\phi$, $\Delta x_\theta \equiv \Delta \mathbf{x} \cdot \hat{\mathbf{e}}_\theta$, and $\Delta z \equiv \Delta \mathbf{x} \cdot \hat{\mathbf{e}}_z = \Delta x_\theta \sin \Upsilon + (\Delta \mathbf{x} \cdot \mathbf{k}_n) \cos \Upsilon / k$. In other words, the effect of the wavefront curvature is to displace the waist of the convergent beam along the wavevector \mathbf{k}_n , and the effect of the source offsets x''_ϕ , x''_θ from $(\mathbf{x}''_{bc})_n$ is to displace the waist along the $(\hat{\mathbf{e}}_\phi)_n$ and $(\hat{\mathbf{e}}_\theta)_n$ directions. In the low NA limit with full pupil illumination, Eqs. (16) and (17) reduce to the standard paraxial result described above.

Figure 9 shows the displacement of a hybrid excited, maximally symmetric, simple cubic bound lattice of period $\sqrt{35}\lambda/2$ in $|\mathbf{e}(\mathbf{x})|^2$, created with 16 internal beams through each of two opposed objectives, and 16 external beams between them. To yield a small sub-zone capable of contributing to a sharp composite zone boundary, $na = 0.08$ was chosen for all 48 convergent beams. Comparison (Fig. 9(b)) of the undisplaced lattice, created with input beams of flat phase, with a lattice displaced by $\Delta \mathbf{x} = (3\hat{\mathbf{e}}_x + 4\hat{\mathbf{e}}_y + 5\hat{\mathbf{e}}_z)\lambda$, created with confined input beams of phase as dictated by Eqs. (16) and (17) and shown in Fig. 9(a), demonstrates that the excitation zone can be translated without affecting the underlying lattice. This is confirmed by the xy plots through the centers of the two zones in Figs. 9(c),(d).

Fig. 10 shows a bound lattice with a composite excitation zone created by the superposition of an $11 \times 11 \times 7$ array of sub-zones of the type shown in Fig. 9. To produce a uniform excitation envelope such as seen in Figs. 10(c) and (d), the spacing between adjacent sub-zones (one lattice period, or $\sqrt{35}\lambda/2$, in Fig. 10) should be significantly smaller than their widths ($2\rho \approx 7\lambda$ in Fig. 9), and the phases of all beams in all sub-zones should be adjusted to yield maximal constructive interference at common lattice points.

A composite excitation zone consisting of Z sub-zones, each of which is in turn comprised of N convergent beams, would appear to require the production and manipulation of NZ distinct beams, or $48 \times 11 \times 11 \times 7 = 40656$ beams for Fig. 10. Fortunately, however, the differences in the propagation directions are so minute between the Z beams in all sub-zones related to the same plane wave of the ideal lattice, that they can be replaced with a single convergent beam given by the superposition of the Z related beams. This beam in turn can be

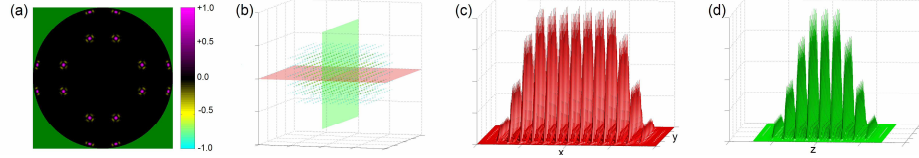


Fig. 10. Composite excitation zone comprised of an $11 \times 11 \times 7$ array of offset sub-zones of the type shown in Fig. 9: a) Superposition factor $\Pi_n(\mathbf{x}'')$ applied to the 16 input beams at one rear pupil; b) Isosurfaces of $0.5 \max[|\mathbf{e}(\mathbf{x})|^2]$ (yellow) and $0.2 \max[|\mathbf{e}(\mathbf{x})|^2]$ (aqua) over $(37\lambda)^3$; c,d) Surface plots of $|\mathbf{e}(\mathbf{x})|^2$ through the xy (red) and yz (green) slice planes, respectively, in (b). Accompanying animation (0.53 MB) shows the variation in $\Pi_n(\mathbf{x}'')$ as the distribution of sub-zones contributing to the overall composite zone is changed.

generated by the superposition of Z input beams either filling a single low na lens (for a superposed external beam), or localized at the same position $(\mathbf{x}''_{bc})_n$ in the rear pupil of an objective (for a superposed internal beam). In either case, the superposed input beam:

$$\mathbf{e}_n^i(\mathbf{x}'', t) = \sum_{m=1}^Z \mathbf{e}_n^i \psi_n(\mathbf{x}'') \exp[i\Phi_n(x'', y'', \Delta \mathbf{x}_m) - i\omega t] \equiv \mathbf{e}_n^i \psi_n(\mathbf{x}'') \Pi_n(\mathbf{x}'') \exp(-i\omega t) \quad (18)$$

has a complex superposition factor $\Pi_n(\mathbf{x}'')$ (e.g., Fig. 10(a)) that could be produced with a spatial light modulator (SLM). The entire bound lattice and its composite excitation zone could then be created with only N beams, related to the N plane waves of the ideal lattice.

7. Conclusions

Using one or more SLMs to define the input beams has advantages in addition to providing a convenient means to shape the excitation zone. As discussed above, they can be used for adaptive optical correction of specimen or substrate induced phase errors, as well as for the simpler tasks of steering the convergent beams to precise positions within the excitation zone, controlling their relative phases to achieve optimal constructive interference at the excitation maxima, and scanning the resulting lattice over one primitive cell for massively parallel, dynamic three-dimensional imaging of a much larger volume.

Furthermore, a pair of SLMs manipulating orthogonally polarized beams can be used to control the polarization \mathbf{e}_n^i as well as the amplitude and phase of the cross-sectional extent $\psi_n(\mathbf{x}'')$ and superposition factor $\Pi_n(\mathbf{x}'')$ of every input beam in a group. This should allow for rapid, programmable control of the lattice symmetry, Wigner-Seitz primitive cell shape, spatial frequency content, overall basis field $\mathbf{e}(\mathbf{x}, t)$, and excitation zone envelope. In turn, this may lead to an unprecedented level of dynamic control over the shape, width, depth, and eigenstate selectivity of the trapping potentials used in optical lattice based quantum simulators and quantum computers. In this regard, it should also be noted that the convergent beam displacement equations (Eqs. (16,17)) can be extended in the full pupil illumination limit to determine an SLM-mediated phase response yielding a steerable, high NA single focus trap capable of loading single atoms into individual potential minima from a reservoir, thereby permitting the creation a defect-free atomic lattice of individually addressable sites.

Sparse composite lattices of widely spaced, tightly confined excitation maxima [24] experimentally generated by the means described here may also open new avenues for several forms of microfabrication. Such lattices in 2D (where all the ideal wavevectors lie on the surface of a single cone) can be created by localized illumination at appropriate points centered on a circle concentric with the rear pupil of a single objective, and can serve as masks of trapping potentials for direct deposition of laser-cooled atoms onto a surface [35-37]. With sufficient cooling, the minimum features sizes so created can be small compared to λ , while the size of each simultaneously written copy of an arbitrarily complex pattern in each primitive cell can be large compared to λ . Similarly, massively parallel fabrication of

aperiodic 3D structures large compared to λ should be possible with 3D sparse composite lattices in a thick photosensitive material. In fact, with basis fields chosen as described in [24], the contrast between each lattice maximum and the surrounding background should be superior to that seen near the focus of a confocal microscope, potentially leading to reduced proximity effects and hence the ability to write more closely packed features without fear of overexposure. Significantly higher axial resolution is also obtained. Two-photon absorption (TPA) photopolymerization [38] could be used to improve the contrast even further and, if used near threshold, might lead to the mass production of large, complex 3D structures having nanometric features. In this regard, we note that the effective coherence length $l \approx c\tau$ of the ultrafast pulses of temporal width τ necessary to achieve TPA naturally leads to a bound lattice excitation zone of similar size, even without spatial confinement of the constituent beams. Finally, although large period sparse composite lattices would appear to be ill suited for the fabrication of photonic crystals with band gaps on the order the wavelength used for their creation, discrete exposure at many points in each primitive cell can create such structures. In fact, recent experiments have aimed at tailoring the optical properties of photonic crystals by controlling the properties of the basis field used in their creation [39], and sparse composite lattices offer an additional degree of control, permitting the creation of complex multi-“atom” bases with unique diffracting properties.

For both quantum optics experiments and live cell imaging, one key issue not yet considered is the simultaneous, efficient, and individualized detection of signal generated at a plurality of excitation maxima across multiple lattice planes. The use of high NA objectives potentially addresses the issue of collection efficiency, but the magnified images of the individual maxima at an image plane become increasingly aberrated for maxima increasingly far from the objective focal plane, reducing the detection resolution and, for spatially filtered signals, the effective collection efficiency. Means to deal with these issues and achieve optimal 3D detection resolution and efficiency will be considered in an upcoming paper [25].

Optical lattice microscopy offers several advantages compared to the established method of multifocal microscopy based on Nipkow disk scanners, either with [40] or without [41] a microlens array to increase the excitation efficiency. First, either method permits massively parallel and hence rapid confocal imaging over a large field of view, but lattice microscopy alone is readily adapted to simultaneous imaging in three dimensions. Second, in lattice microscopy, an arbitrarily large 2D or 3D array of excitation foci of controllable spacing and symmetry is generated with a finite number of beams over a controllable volume, rather than a fixed 2D array of foci spread over a fixed field, created with a fixed number of excitation apertures and/or microlenses. Third, adaptation of 4π excitation and/or detection to conventional multifocal microscopy would be challenging, but is readily accomplished with opposed objectives in lattice microscopy, to yield a substantial improvement in axial resolution. Fourth, slight improvement in transverse resolution and elimination of the axial side-lobes plaguing 4π microscopy is possible using hybrid excitation (Fig. 7). Fifth, since the polarization of every input beam contributing to a lattice can be individually optimized, greater polarization purity at the foci is possible than in multifocal microscopy, where constant polarization over the rear pupil leads to depolarization effects at the foci in a high NA system [42]. Finally, in typically weakly absorbing biological specimens, the energy flow and hence photobleaching propensity is constant in every plane throughout the entire thickness of the specimen for confocal or multifocal illumination, rendering these methods wasteful of the limited bleaching-dictated photon budget, and leading to significant out-of-plane autofluorescence and loss of detection sensitivity at the desired focal plane. On the other hand, the optimization of constructive interference at the excitation foci in lattice microscopy and the partial destructive interference at other points in each primitive cell lead to significantly higher conversion efficiency of emitted photons to usable signal. These comparisons will be considered in quantitative detail in a forthcoming paper [43].